Figure S1 (related to Figure 1)

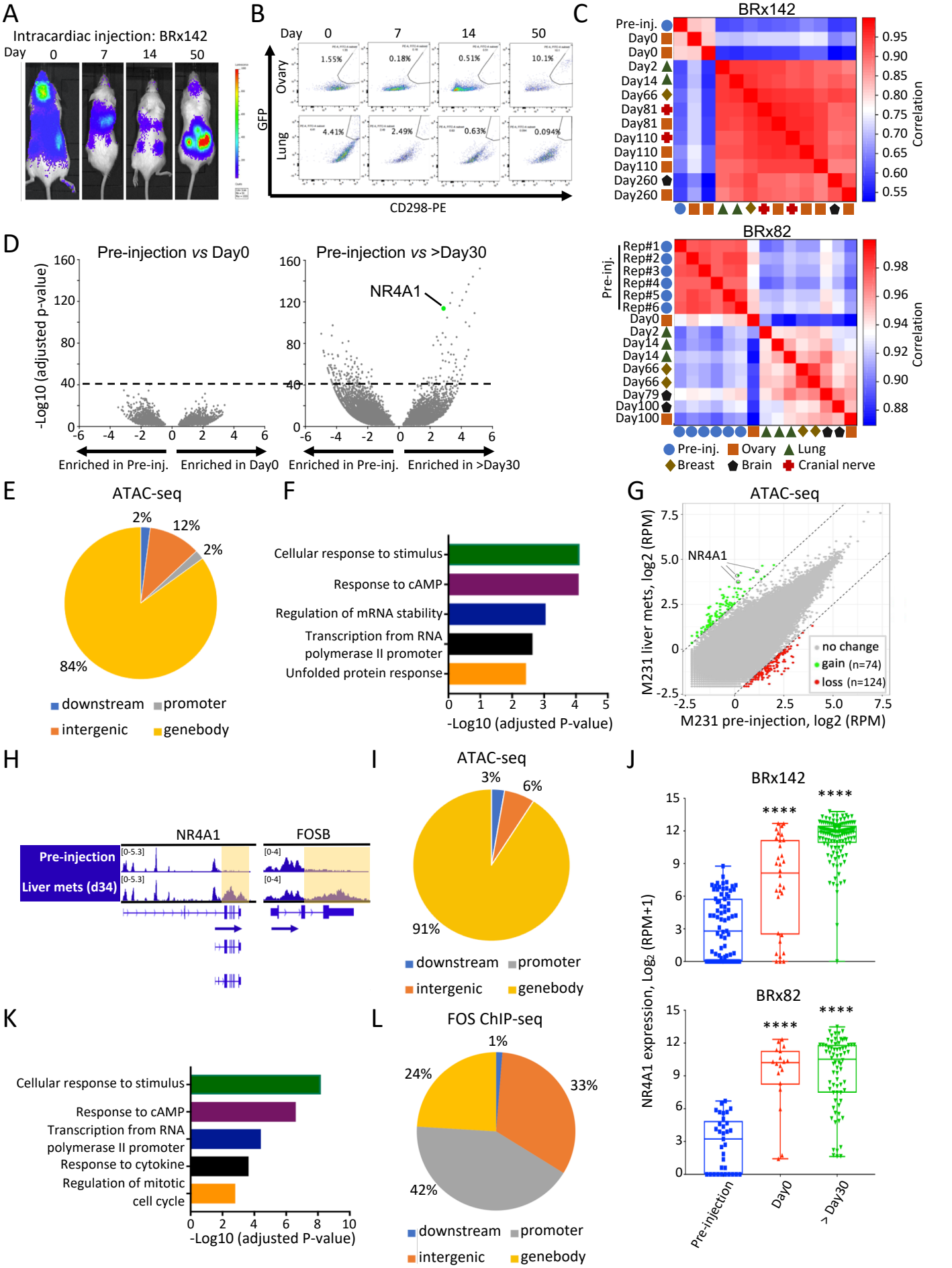

Figure S2 (related to Figure 2)

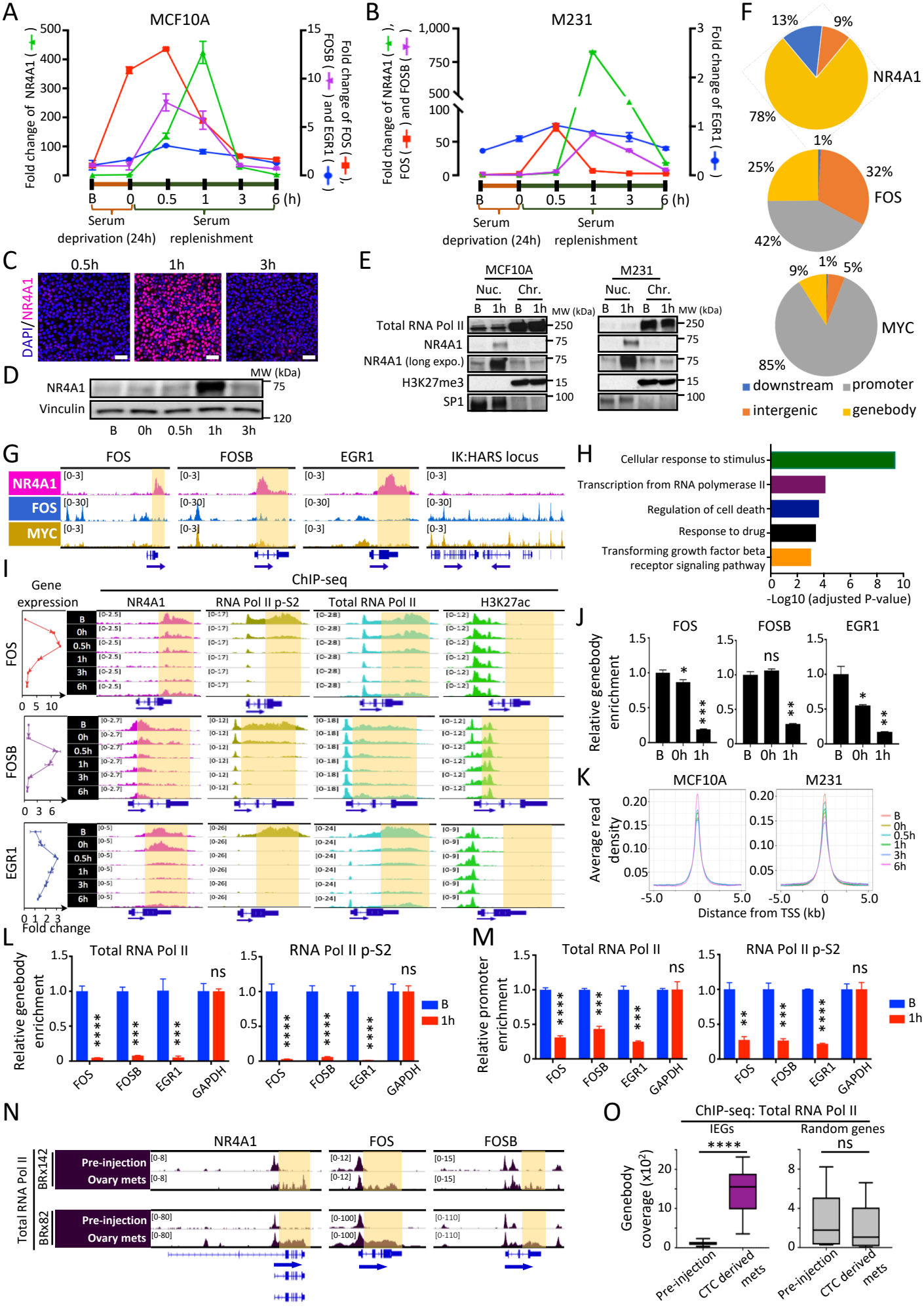

Figure S3 (related to Figures 2 and 3)

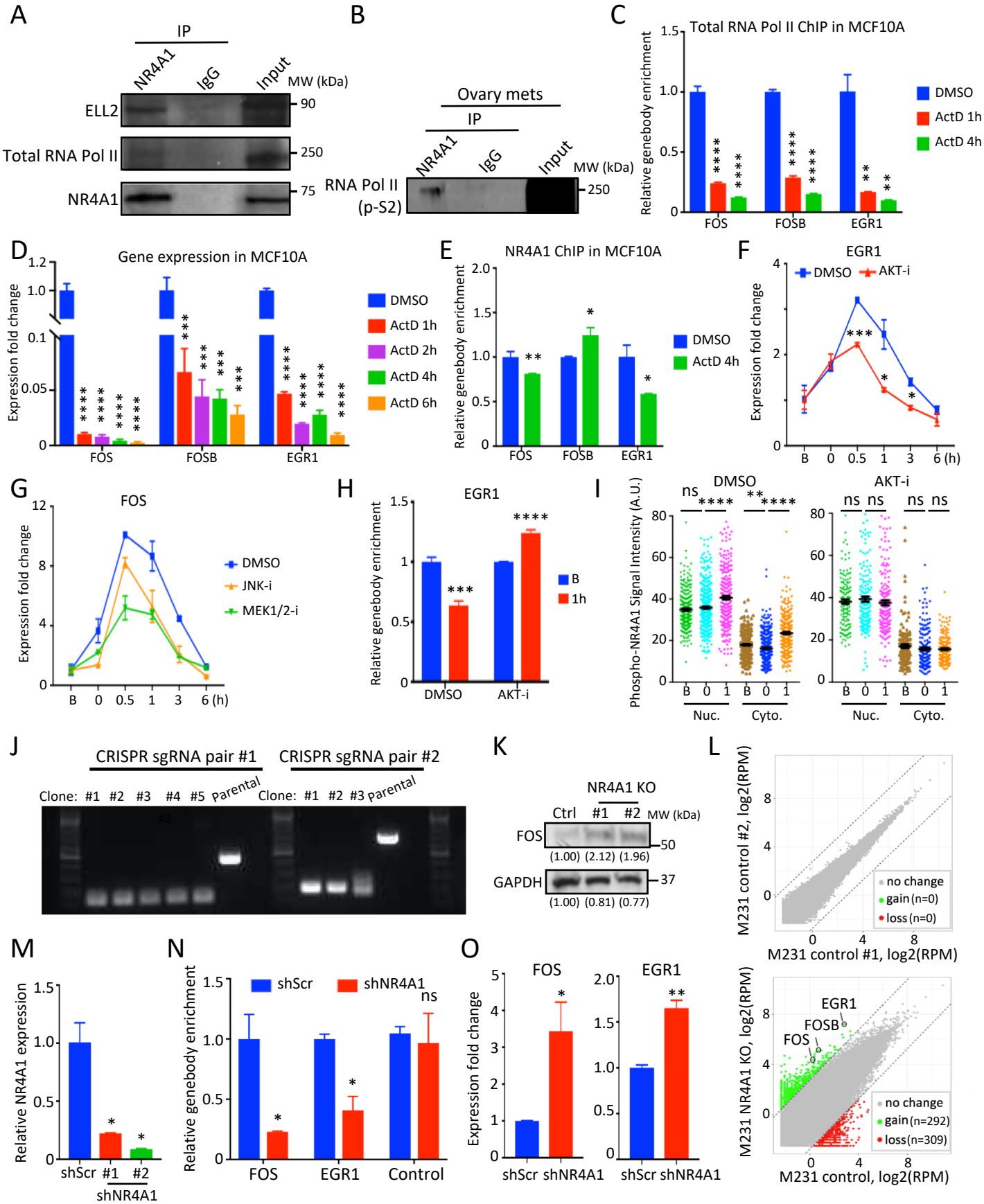

Figure S4 (related to Figures 3 and 4)

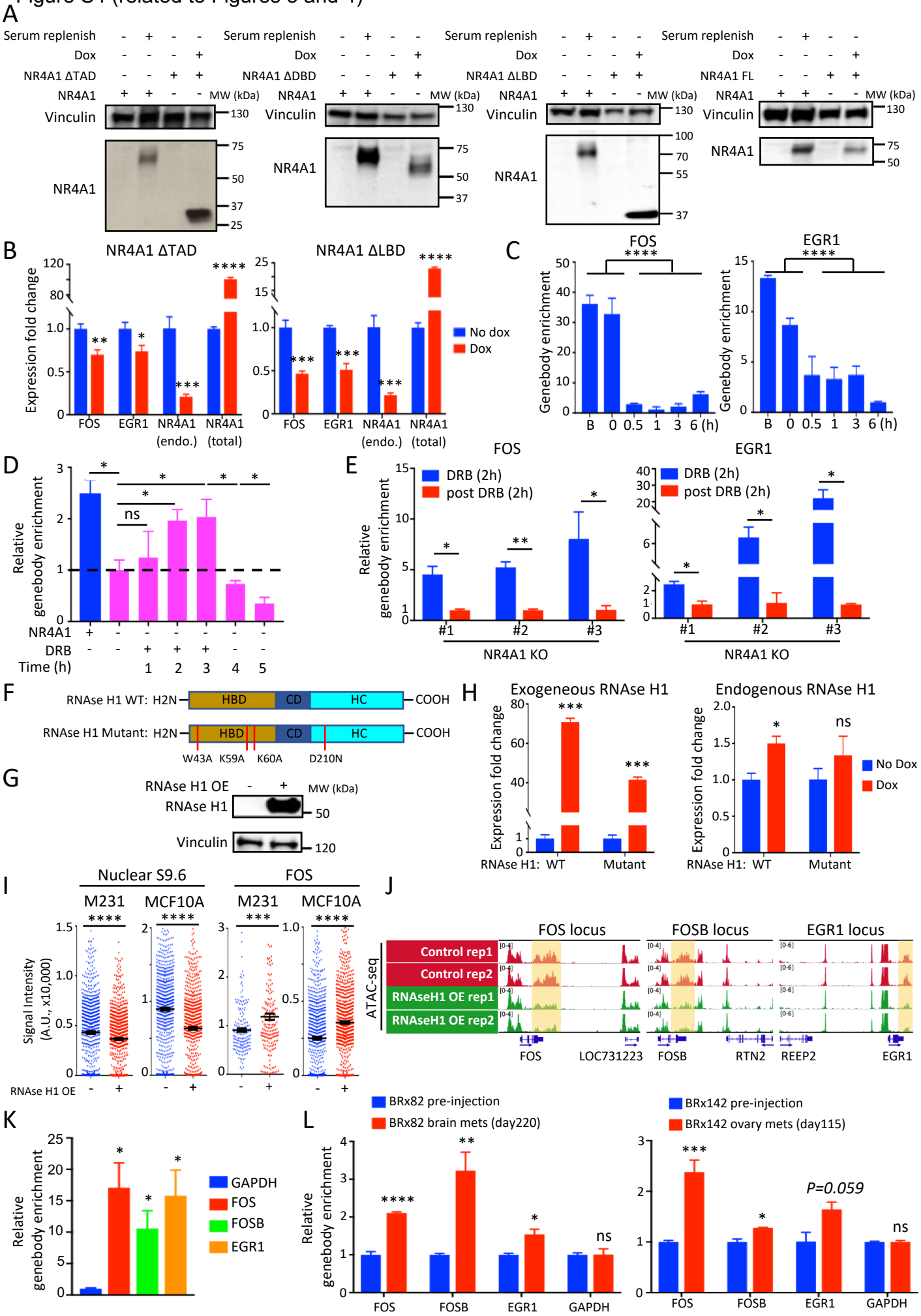

Figure S5 (related to Figure 5)

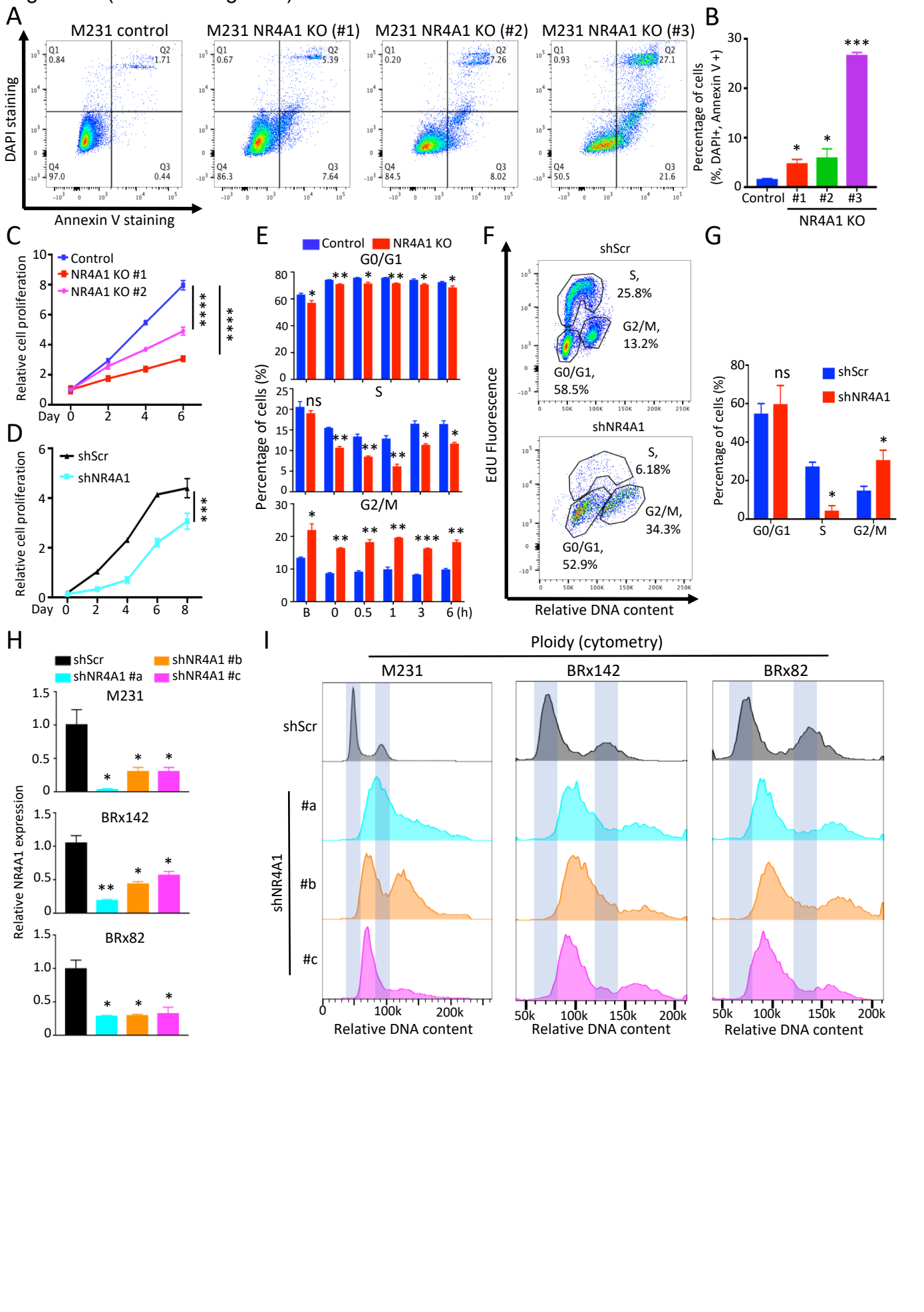

Figure S6 (related to Figure 5)

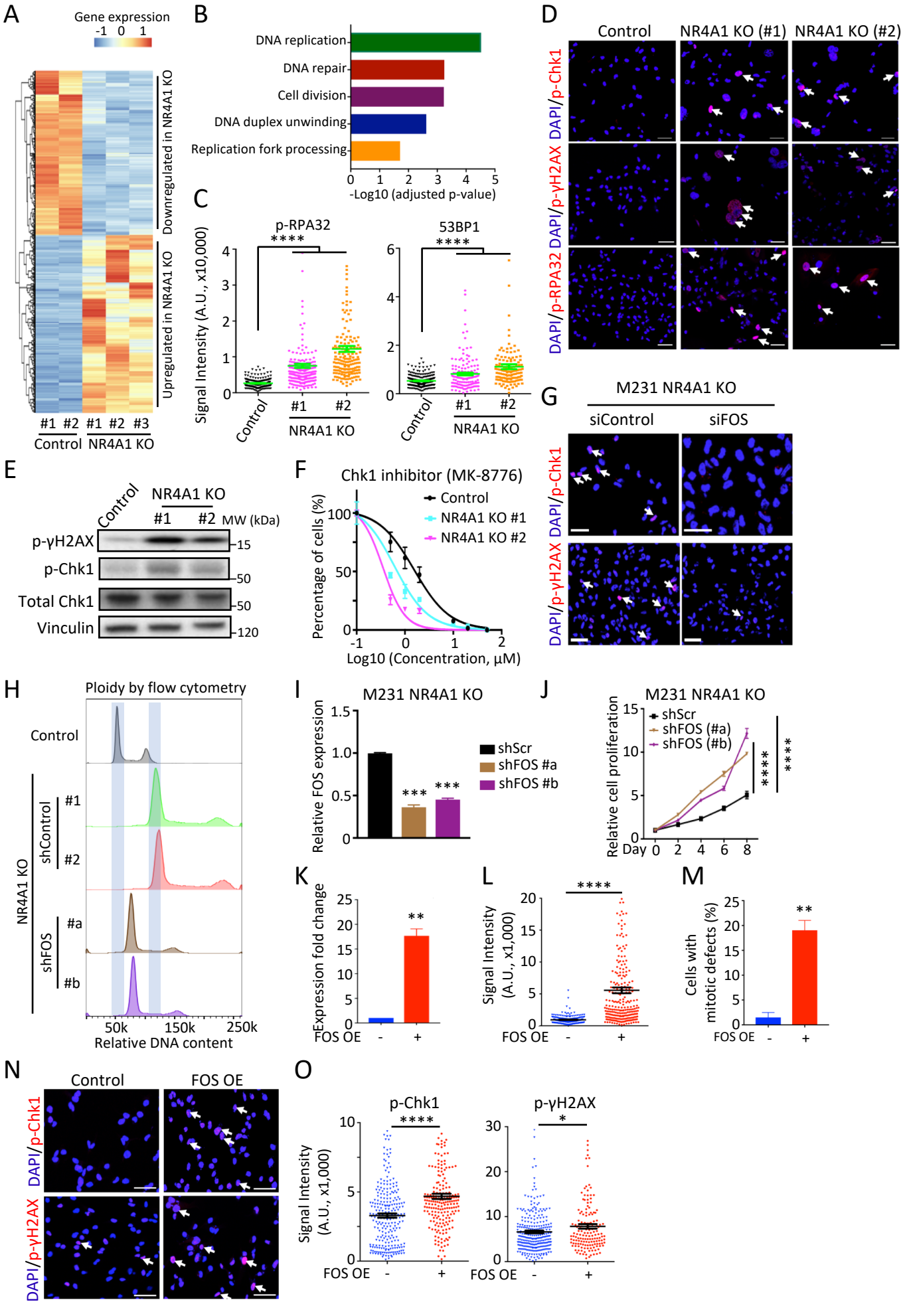

Figure S7 (related to Figures 6 and 7)

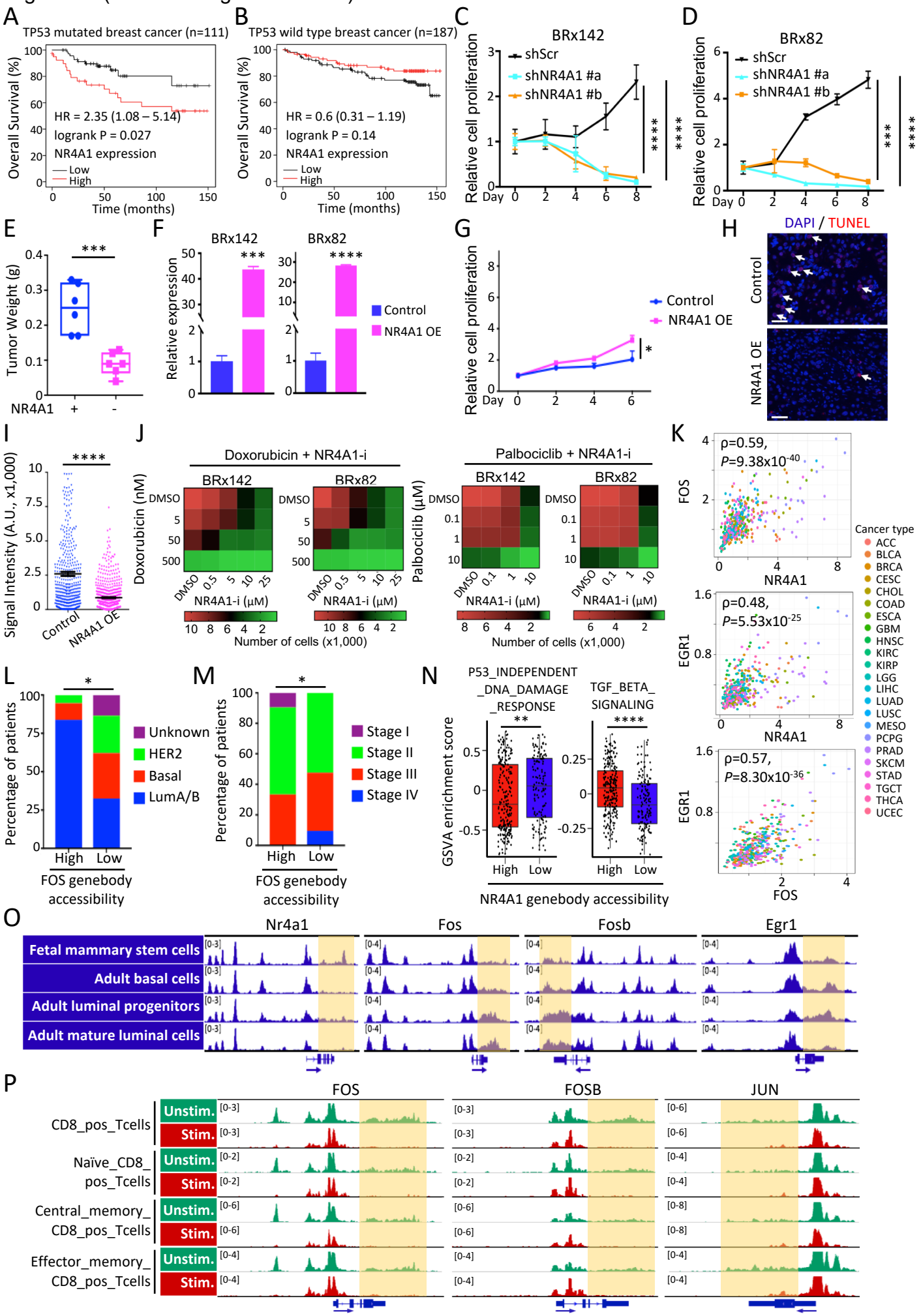

Supplementary Figure Legends

Figure S1 Temporal dynamics of chromatin accessibility in tumor cells during *in vivo* tumor initiation. Related to Figure 1.
(A) We inoculated BRx142 and BRx82 CTC lines via intracardiac injection into NSG mice to generate metastatic lesions. These cultured CTCs were originally isolated from patients with metastatic hormone-receptor positive, *TP53*-mutant breast cancer (Jordan et al., 2016), and they were tagged with GFP and luciferase for real-time *in vivo* imaging. An hour after intracardiac inoculation (day 0), and at serial intervals thereafter, mouse tissues were harvested, subjected to single-cell dissociation, and individual tumor cells were collected by fluorescence-activated cell sorting (FACS) for expression of both GFP and the human-specific marker CD298 (Lawson et al., 2015). To search for chromatin-associated changes at early time points in tumor formation, we applied Assay for Transposase Accessible Chromatin using sequencing (ATAC-seq) and Chromatin Immunoprecipitation followed by sequencing (ChIP-seq) to grouped FACS-purified tumor cell populations, comparing cells retrieved from tissues at different time points and pre-inoculation CTCs. Figure shows bioluminescence imaging (IVIS) of a representative mouse, showing tumor cell-derived luciferase signal at various time points after intracardiac injection of BRx142 cultured CTCs. At day 50, metastatic tumors are evident in both ovaries and brain. **(B)** Gating of CD298 (human cell-specific marker) and GFP (transfection marker) double positive CTC-derived tumor cells, recovered from mice at serial intervals after intracardiac injection, following single cell dissociation of lung and ovarian tissues . For day0, tissues were collected 1 hour after intracardiac injection. **(C)** Correlation heatmaps of the ATAC-seq among pre-injection CTCs and CTCs retrieved from mouse tissue at different timepoints after intracardiac inoculation for both BRx142 (upper panel) and BRx82 (bottom panel). High correlation is observed across six biological replicates of BRx82 pre-injection CTCs, demonstrating the reproducibility and robustness of ATAC-seq technique. Color key from blue to red indicates correlation from low to high, respectively. **(D)** Volcano plots showing minimal chromatin accessibility changes between pre-injection BRx82 CTCs and CTC retrieved from ovary at day0; a small subset of genes show dramatic differences in ATAC-seq signal between pre-injection CTCs and CTCs recovered from ovary metastasis at day100 (>day30). *NR4A1* is indicated as one of the top hits. **(E)** Pie chart showing the distribution of genomic regions gaining chromatin accessibility during metastasis in both CTC cell lines, with marked predominance (approximately 84%) residing within genebody regions. **(F)** Cellular pathways identified using gene ontology analysis applied to genes with acquired genebody chromatin accessibility (ATAC-seq) in CTC-derived metastases. “Cellular response to stimulus” denotes common correlates of immediate early gene expression. **(G)** To extend the findings from patient CTC-derived tumors to a prototypical highly tumorigenic breast cancer cell line, we repeated the intracardiac inoculations using the triple negative breast cancer cell line MDA-MB-231 (M231). ATAC-seq of GFP-tagged M231 cells retrieved after 30 days from mouse liver metastasis also shows acquisition in early tumor lesions of open chromatin domains, restricted to the genebody and 3’-UTR of multiple IEGs, which are absent from cells retrieved from mouse tissues at day 0 and pre-injection cells. Scatter plot showing chromatin accessibility changes in M231-derived metastasis (liver), following

intracardiac injection (representative mouse). Each dot represents a 2 kb tile in the genome, green dots indicate regions gaining chromatin accessibility, red dots indicate loss of chromatin accessibility, while grey dots indicate no significant change. *NR4A1* shows significant gain of ATAC-seq signal. **(H)** IGV tracks showing gain of chromatin accessibility at genebody or 3'-UTR of IEGs (*NR4A1, FOSB*) in M231-derived metastases (liver) (data from one representative mouse) **(I)** Pie chart showing the genomic regions that gain of chromatin accessibility (ATAC-seq) in M231-derived metastases, following intracardiac injection, virtually all of which (>91%) are within genebody regions. **(J)** Boxplot shows induction of *NR4A1* mRNA in single BRx142 CTCs (upper panel) and BRx82 CTCs (bottom panel) from pre-injection, to day0, to >day30 recovered from mouse ovarian metastasis (data from representative mouse). *NR4A1* RNA increases from pre-injection CTCs to cells retrieved from early ovarian tumors (>day 30) (BRx142: 104-fold change, P<9.69E-27; BRx82: 113-fold change, P<1.5E-06). Each dot represents a single cell. ****P<0.0001 by two-tailed Student's t-Test, n>17 single cells. **(K)** Gene ontology analysis of genes with NR4A1 genebody binding (ChIP-seq), in both BRx142 and BRx82 CTC-derived metastases, with "cellular response to stimulus" (P=6.5E-9) as the most significant pathway, and 64% of identified genes encoding known IEGs (see Table S3). NR4A1 binding to IEG genebodies is observed in CTC-derived tumors, but not in preinjection CTCs, paralleling the observation of open chromatin domains (originally identified by ATAC-seq) acquired during early tumorigenesis. **(L)** Pie chart showing genomic regions with enrichment for FOS binding in BRx82 CTC-derived ovarian metastases**.** In contrast to the unexpected predominance of genebody occupancy by NR4A1, FOS shows primarily the characteristic transcription factor binding to promoters and transcriptional start sites (TSS).

Figure S2 NR4A1 restrains RNA Polymerase II transcriptional elongation at the genebody of IEGs. **Related to Figure 2.**

(A-B) IEG expression in MCF10A cells (panel **A**) and M231 cells (panel **B**) grown under baseline serum-containing conditions ("B"), after 24 hours of serum deprivation (0h) and following serum replenishment (0.5, 1, 3 and 6h). RNA quantified by real time qPCR. Error bar represents SD, n=3. **(C)** Immunofluorescence staining for NR4A1 in MCF10A cells at 0.5, 1 and 3 hours after serum replenishment to demonstrate tight peak of transient protein expression. Scalebar, 50 μM. **(D)** Western blot showing rapid induction of NR4A1 protein after serum replenishment of starved MCF10A cells. Serum-replete baseline (B), 24 hours serum deprivation (0h), and serum replenishment (0.5, 1, 3h). Vinculin, loading control. **(E)** Western blots showing the nucleoplasmic (Nuc.) and chromatin-bound (Chr.) proteins for NR4A1 and total RNA Pol II under baseline culture condition ("B") and serum replenishment condition (1h) in both MCF10A and M231 cells. H3K27me is used as marker for chromatin fraction; SP1 (Specificity protein 1) is a marker for nucleoplasm. **(F)** Pie chart of ChIP-seq data, showing genomic regions with enrichment in binding by different IEGs, including NR4A1, FOS and MYC in MCF10A cells grown under baseline serum conditions. Notably, only NR4A1 demonstrates predominant genebody occupancy, while FOS and MYC show characteristic binding to gene promoters. **(G)** IGV tracks showing NR4A1 (pink), FOS (blue) and MYC (yellow) protein binding at genomic loci of

three representative IEGs (*FOS, FOSB*, *EGR1)* in MCF10A cells under baseline, serum-replete conditions. The IK:HARS locus is shown as a representative control region demonstrating characteristic promoter binding by FOS and MYC, but not by NR4A1. **(H)** Gene ontology analysis of genes with NR4A1 binding in MCF10A cells under baseline, serum-replete conditions. "Cellular response to stimulus" is enriched for IEG signaling pathways. **(I)** IGV tracks showing ChIP binding dynamics of NR4A1 (pink), RNA Pol II phospho S2 (olive), total RNA Pol II (cyan) and H3K27ac (green) at three IEG loci (*FOS*, *FOSB*, *EGR1*). Accumulation of NR4A1, RNA Pol II p-S2 and total RNA Pol II ChIP reads at IEG genebody and 3'-UTR is highlighted in shaded yellow. The distribution of both phospho-S2 and total RNA Pol II mirror that of NR4A1, whereas the enhancer activation H3K27ac histone mark is undetected at NR4A1, RNA Pol II p-S2 and total RNA Pol II-bound regions. The reduction in genebody and 3'UTR binding by NR4A1, RNA Pol II p-S2 and total RNA Pol II is serially monitored in MCF10A cells, as they transition from baseline serum-replete culture ("B"), to 24 hour serum starvation (0h), and serum replenishment (0.5, 1, 3, and 6h). RNA expression levels for each IEG (*FOS, FOSB, EGR1*) is shown in the extreme left panel, showing anti-correlation of mRNA expression with both NR4A1 and RNA Pol II accumulation at the IEG genebody. Genomic structures are shown under each set of IGV tracks. **(J)** Analysis of M231 cells by ChIP-qPCR, showing the serial reduction in NR4A1 binding at genebody regions of IEGs (*FOS, FOSB*, *EGR1)* under basal serum conditions ("B"), 24 hour serum starvation (0h), and serum replenishment (1h). Error bar denotes SD. *P<0.05; **P<0.01; ns, not significant, by two-tailed Student's t-Test, n=2. **(K)** Genome-wide RNA Pol II enrichment at transcriptional start sites (TSS) in both MCF10A and M231 cells, demonstrating the generally expected distribution, distinct from that observed at IEGs. **(L-M)** Bar graphs showing occupancy of total RNA Pol II and RNA Pol II p-S2 in MCF10A cells at IEG genebody (panel **L**) and promoter (panel **M**) regions under baseline conditions ("B") and serum replenishment of starved cells (1h), using a second set of ChIP antibodies against total RNA Pol II and RNA Pol II p-S2 (see Methods). Error bar represents SD. **P<0.01; ***P<0.001; ****P<0.0001 by two-tailed Student's t-Test, n=3. **(N)** IGV tracks showing total RNA Pol II ChIP-seq signal at genebodies of *NR4A1*, *FOS* and *FOSB* in ovarian metastases derived from two different CTC lines (BRx142, BRx82), but not in either re-injection CTCs. **(O)** Boxplots showing gain of RNA Pol II occupancy at six IEG genebody regions (*FOS, FOSB, EGR1, JUN, JUNB* and *JUND*) in CTC-derived tumors, but not at six randomly selected genebodies across the genome. ****P<0.0001; ns, not significant by two-tailed Student's t-Test, n=6.

Figure S3 *NR4A1* interacts with RNA Pol II and its suppression reduces RNA Pol II stalling and triggers IEG transcription. **Related to Figures 2 and 3.**
(A) Co-immunoprecipitation followed by western blot, showing protein association between NR4A1 and RNA Pol II elongation factor, ELL2, and total RNA Pol II in MCF10A cells under baseline culture conditions. **(B)** Co-immunoprecipitation followed by western blot, showing protein association between NR4A1 and RNA Pol II (CTD phospho S2) in CTC-derived ovarian metastasis. **(C)** Total RNA Pol II ChIP-qPCR assay showing sequential reduction of RNA Pol II occupancy at IEG genebodies after actinomycin (ActD) treatment in MCF10A cells. Error bar represents SD. **P<0.01; ****P<0.0001, by two-

tailed Student's t-Test, n=3. **(D)** Gene expression analysis showing sequential decrease in IEG mRNA expression after actinomycin (ActD) treatment. Error bar represents SD. ***P<0.001; ****P<0.0001, by two-tailed Student's t-Test, n=3. **(E)** NR4A1 ChIP-qPCR analysis showing modest changes of NR4A1 binding at IEG genebodies after actinomycin (ActD) treatment. Error bar represents SD. *P<0.05; **P<0.01, by two-tailed Student's t-Test, n=3. **(F)** We tested a series of kinase inhibitors targeting AKT (Ipatasertib), MEK1/2 (U0126), p38 MAPK (SB203580), and JNK (SP600125) for their effect on both serum-induced IEG expression and NR4A1 chromatin localization (see Methods). Among these, AKT inhibition, and to a lesser extent MEK1/2 inhibition, suppresses IEG expression upon serum stress in MCF10A. Figure shows suppression of *EGR1* induction following AKT-inhibitor treatment during serum withdrawal (0h) and serum replenishment (0.5, 1, 3, 6h), compared with baseline ("B"). Error bar represents SD. *P<0.05; ***P<0.001; by two-tailed Student's t-Test, n=2. **(G)** Suppression of *FOS* induction following treatment with JNK-inhibitor (SP600125) or MEK1/2-inhibitor (U0126), during serum withdrawal (0h) and serum replenishment (0.5, 1, 3, 6h), compared with baseline ("B"). **(H)** ChIP-qPCR showing persistence of NR4A1 binding at EGR1 genebody after serum replenishment (1h) in serum-starved MCF10A cells treated with AKT-inhibitor, compared with its reduction in DMSO controls. Error bar represents SD. *P<0.01; ****P<0.0001; by two-tailed Student's t-Test, n=3. **(I)** Quantitative analysis of single cell immunofluorescent staining of phospho-NR4A1 (using a second antibody recognizing phospho-serine 351 NR4A1), demonstrating reduction in NR4A1 phosphorylation in AKT-i treated MCF10A cells at 1h post serum stimulation. Signal intensity is quantified based on the nuclear (Nuc.) and cytoplasmic (Cyto.) fluorescence (see Methods). Error bar denotes SEM. **P<0.01; ****P<0.0001; ns, not significant, by two-tailed Student's t-Test, n>140 single cells**. (J)** Genomic PCR validation of CRISPR-mediated *NR4A1* gene deletion in M231 cells, using two different pairs of guide-RNA sequences (see Methods). **(K)** Western blot showing upregulation of FOS protein expression in two clones of M231 *NR4A1*-null cells (KO) cultured under baseline conditions (GAPDH, loading control). The band intensities quantified by ImageJ are provided numerically below. **(L)** Scatter plot showing gain of PRO-seq signal indicating nuclear run-on activity and RNA polymerase processing at IEGs (*FOS, FOSB, EGR1*) in *NR4A1*-null M231 cells, compared with parental controls, cultured under baseline serum-replete conditions (fold change >6.5 indicates PRO-seq signal gain or loss). Each dot represents a 2kb tile; green dots or red dots represent regions with gain or loss of PRO-seq signal in M231 NR4A1-null cells, respectively; grey dots indicate no significant change. Number of genes that gained or lost PRO-seq signal is indicated**. (M)** Bar graph showing *NR4A1* knockdown efficiency in MCF10A cells, using two different shRNA constructs (see Methods). RNA quantitation by real time qPCR. Error bar represents SD. *P<0.05 assessed by two-tailed Student's t-Test, n=2. **(N)** Bar graph showing reduced total RNA Pol II ChIP-qPCR signal at genebody regions of *FOS* and *EGR1* in MCF10A cells subjected to shRNA-mediated *NR4A1* knockdown and grown under baseline serum-replete conditions, compared with scramble controls (shScr). GAPDH, control genebody locus. Error bar represents SD. *P<0.05; ns, not significant, by two-tailed Student's t-Test, n=2. **(O)** Bar graph showing upregulation of *FOS* and *EGR1* mRNA after shRNA-mediated *NR4A1* knockdown in MCF10A cells grown under baseline conditions. Error bar represents SD. *P<0.05; **P<0.01 by two-tailed Student's t-Test, n=2.

Figure S4 *NR4A1* deletion resolves R-loops at IEG genebody and enables IEG transcription. **Related to Figures 3 and 4.**

(A) Western blots showing doxycycline (Dox) induction of full length (FL) NR4A1 and NR4A1 proteins with deletions of different functional domains (NR4A1 ΔTAD, NR4A1 ΔDBD, NR4A1 ΔLBD), at levels comparable to that of endogenous NR4A1 following serum stimulation. Vinculin, loading control. **(B)** Preserved suppression of IEG expression after doxycycline-inducible expression of NR4A1 proteins with either transactivation domain (NR4A1 ΔTAD) or ligand binding domain (NR4A1 ΔLBD) deletions in NR4A1-null M231 cells. Total *NR4A1* expression is shown to confirm induction of ectopic construct, compared with the mutant endogenous transcript . Error bar represents SD. *P<0.05; **P<0.01; ***P<0.001; ****P<0.0001, by two-tailed Student's t-Test, n=3. **(C)** S9.6 DRIP-qPCR assay showing serial reduction in R-loop signal present at the *FOS* and EGR1 genebodies in MCF10A cells grown under basal serum conditions ("B"), after 24 hour serum withdrawal (0h), and following serum refeeding (0.5, 1, 3, 6h). Error bar represents SD. ****P<0.0001 by two-tailed Student's t-Test, n=4. **(D)** Total RNA Pol II ChIP-qPCR showing reversible enrichment of RNA polymerase along the *FOS* genebody in *NR4A1*-null M231 cells after transient treatment with the transcriptional inhibitor DRB (pink), recapitulating the transcriptional elongation block mediated by NR4A1 binding (see Methods). As control, reduction of RNA Pol II accumulation at the *FOS* genebody in parental M231 cells (blue), compared with *NR4A1*-null cells. Error bar indicates SD. *P<0.05; ns, not significant, by two-tailed Student's t-Test, n=3. **(E)** S9.6 DRIP-qPCR showing R-loop signal at genebody regions of *FOS* and *EGR1* in three independent NR4A1-KO M231 cells, following treatment with the transcriptional inhibitor DRB (2h) or after DRB withdrawal (2h), recapitulating the NR4A1 effect. Error bar indicates SD. *P<0.05; **P<0.01 by two-tailed Student's t-Test, n=3. **(F)** Schematic representation of wild type (WT) and mutant RNAse H1 constructs, with three missense mutations (W43A, K59A, K60A) in the DNA/RNA Hybrid Binding Domain (HBD), and one missense mutation (D210N) in the Catalytic domain (HC). CD denotes the Connection Domain. **(G)** Western blot showing ectopic *in vivo* expression of RNAse H1 protein, Vinculin, loading control. **(H)** Gene expression analysis of exogeneous and endogenous RNAse H1 expression after lentiviral transduction of either RNAse H1 wild type or mutant constructs. Error bar represents SD. *P<0.05; ***P<0.001; ns, not significant, by two-tailed Student's t-Test, n=3. **(I)** Quantitation of single cell immunofluorescence staining for nuclear S9.6 and FOS, following Dox-inducible expression of RNAse H1 in either M231 and MCF10A cells cultured under baseline conditions, showing both reduction in R-loops (nuclear S9.6) and associated increase in FOS expression. Error bar denotes SEM. ***P<0.001; ****P<0.0001 by two-tailed Student's t-Test, n>150 single cells. **(J)** IGV tracks showing ATAC-seq signal at IEG (*FOS, FOSB, EGR1*) genebody regions in MCF10A cells cultured under basal serum conditions (two biological replicates; red), and the reduction in ATAC-seq signal following Dox-inducible expression of RNAse H1 (OE; two replicates; green). IEG genebody and 3'-UTR regions are highlighted in shaded yellow. No changes are observed in neighboring genes for each IEG locus. **(K)** S9.6 DRIP-qPCR assay showing enrichment of R-loop signal at IEG genebody regions in BRx142 CTC-derived metastases, compared with a control genebody locus (GAPDH). Error bar denotes SD. *P<0.05 by

two-tailed Student's t-Test, n=3. **(L)** H3K27me3 ChIP-qPCR assay showing enrichment of repressive histone marks at IEG (*FOS, FOSB, EGR1*) genebodies in CTC-derived metastases, compared with pre-injection CTCs for both BRx82 and BRx142 CTCs (GAPDH control). Error bar represents SD. *P<0.05; **P<0.01; ***P<0.001; ****P<0.0001; ns, not significant, by two-tailed Student's t-Test, n=3. The statistical significance of H3K27me3 occupancy at EGR1 genebody between BRx142 pre-injection and BRx142 derived ovarian tumor is marginal (P=0.059).

Figure S5 Suppression of *NR4A1* impairs proliferation and triggers replication stress. **Related to Figure 5.**
(A-B) Flow cytometric analysis of cell apoptosis by dual staining for DAPI and Annexin V in parental M231 controls versus three *NR4A1*-null M231 clones (KO) (panel **A**), with quantitation of apoptotic cells (percentage of double positive cells; panel **B**). **(C)** *In vitro* cell proliferation of two independent CRISPR-mediated *NR4A1*-null M231 clones (KO #1,2), compared with parental control. All cells were cultured under baseline serum conditions. Error bar indicates SD. ****P<0.0001 by two-tailed Student's t-Test, n=4. **(D)** *In vitro* cell proliferation assay in MCF10A following shRNA-mediated *NR4A1* suppression, compared with scrambled shRNA control (shScr). Error bar indicates SD. ***P<0.001 by two-tailed Student's t-Test, n=4. Cells were grown under baseline serum conditions. **(E)** Cell cycle analysis of control versus *NR4A1*-knockout M231 cells under baseline culture conditions ("B"), and following 24 hours serum withdrawal (0h), and serum replenishment (0.5h, 1h, 3h and 6h). GO/G1, S and G2/M cell cycle phases determined by EdU incorporation assay. Error bar denotes SD. *P<0.05; **P<0.01; ***P<0.001; ns, not significant, by two-tailed Student's t-Test, n=2. **(F)** EdU incorporation followed by flow cytometric assay, showing the reduction in S phase and accumulation in G2/M phase after *NR4A1* knockdown in MCF10A cells**. (G)** Cell cycle distribution of MCF10A cells after shRNA-mediated *NR4A1* knockdown, versus scramble control (shScr), showing a reduction in S phase fraction and accumulation of cells in G2/M phase. Error bar indicates SD. *P<0.05; ns, not significant, by two-tailed Student's t-Test, n=2. **(H)** Bar graph showing *NR4A1* knockdown efficiency in M231 cells, BRx142 CTCs and BRx82 CTCs using three different shRNA constructs (#a-c). Error bar indicates SD. *P<0.05; **P<0.01 by two-tailed Student's t-Test, n=2. **(I)** DNA ploidy analysis by flow cytometry, showing gain of DNA content and high level of aneuploidy after suppression of *NR4A1* using three different shRNA sequences in M231 cells, and in BRx142 and BRx82 CTCs. X-axis indicates relative DNA content by PI staining.

Figure S6 Deregulated *FOS* expression mediates replication stress in NR4A1-null cells. **Related to Figure 5.**
(A) Heatmap representation of RNA-seq analysis, showing differentially expressed genes in three independent CRISPR-derived *NR4A1*-null M231 clones, versus two parental control clones. Color code from blue to red indicates low to high expression, respectively. **(B)** Gene ontology analysis of genes downregulated in M231 cells after *NR4A1* knockout. **(C)** Quantitation of individual cells with positive phospho-RPA32 and 53BP1 foci, indicating DNA damage signaling, in two *NR4A1*-null M231 clones (KO #1, #2), versus control parental cells. Error bar in green denotes SEM. ****P<0.0001 by two-tailed

Student's t-Test, n>100 single cells. Image quantification was carried out by ImageJ software. **(D)** Representative immunofluorescence staining for the DNA damage response markers phospho-Chk1, phospho-γH2AX and phospho-RPA32 in two *NR4A1*-null M231 clones (KO #1, #2). DAPI nuclear staining. Arrows indicate cells with high level of nuclear staining. Scalebar, 50 μM. **(E)** Activation of DNA damage response pathway, as shown by Western blots for phospho-γH2AX (Vinculin control) and phospho-Chk1 (total Chk1 control) in two independent clones of *NR4A1*-null M231 cells (KO #1, #2), compared with parental controls. (**F)** Increased sensitivity of two independent *NR4A1*-null M231 clones to the Chk1 inhibitor MK-8776, compared with parental control. Error bar indicates SD, n=4. Y-axis represents relative cellular viability; x-axis shows log10 drug concentrations. **(G)** Resolution of DNA damage signaling in *NR4A1*-null M231 cells, following siRNA-mediated *FOS* knockdown, compared with siControl, as measured by immunofluorescence staining for phospho-Chk1 and phospho-γH2AX, along with DAPI nuclear staining. Scalebar, 50 μM. **(H)** DNA ploidy analysis by flow cytometry, showing resolution of aneuploidy in *NR4A1*-null M231 cells following suppression of *FOS* expression using two different shRNA sequences (shFOS #a-#b), versus shRNA controls (shControl #1-2) and parental M231 control. X-axis represents relative DNA content in cells after PI staining. **(I)** Bar graph showing shRNA-mediated knockdown efficiency of *FOS* using two shRNA constructs (#a-b) in *NR4A1*-null M231 cells. Error bar denotes SD. ***P<0.001 by two-tailed Student's t-Test, n=2. **(J)** Reversal of *in vitro* cell proliferation defect in *NR4A1*-null M231 cells, following knockdown of *FOS* using two different shRNA constructs (#a-b). ****P<0.0001 by two-tailed Student's t-Test, n=4. **(K)** Bar graph demonstrating RNA level of ectopic *FOS* overexpression in M231 cells using qPCR. Error bar denotes SD. **P<0.01 by two-tailed Student's t-Test, n=2. **(L)** Single cell quantification of FOS protein expression in M231 cells with ectopic expression of *FOS*, versus parental controls, using immunofluorescence staining. Error bar indicates SEM. ****P<0.0001, by two-tailed Student's t-Test, n>200 single cells**. (M)** Bar graph showing percentage of M231 cells with gross mitotic defects, following ectopic expression of *FOS* (FOS OE), versus untransfected parental controls. Error bar indicates SD. **P<0.01 by two-tailed Student's t-Test, n=3 independent microscopic fields. **(N)** Immunofluorescence staining showing activation of replication stress and DNA damage markers phospho-Chk1 and phospho-γH2AX, along with DAPI nuclear staining, in M231 cells with ectopic expression of *FOS* (FOS OE), versus untransfected controls. Scalebar, 50 μM. **(O)** Quantification of M231 cells with positive phospho-Chk1 and phospho-γH2AX foci, following ectopic expression of *FOS*, versus untransfected controls. Error bar denotes SEM. *P<0.05; ***P<0.001 by two-tailed Student's t-Test, n>150 single cells.

Figure S7 *NR4A1* and IEG open chromatin domains across human cancers. Related to Figures 6 and 7.

(A-B) Kaplan-Meier plots showing inverse correlation of *NR4A1* expression in tumors versus overall survival in patients with *TP53*-mutated breast cancer (panel **A**), but not in patients with *TP53*-wild type breast cancer (Panel **B**). Data are reanalyzed from KMplotter database (https://kmplot.com/analysis/). **(C-D)** *In vitro* cell proliferation of BRx142 CTCs (panel **C**) and BRx82 CTCs (panel **D**) following *NR4A1* knockdown using either of two independent shRNA sequences (shNR4A1 #a, #b), compared with parental control (shScr). Statistical significance was assessed by two-tailed Student's t-Test. ***P<0.001;

****P<0.0001, n=4. **(E)** Weight of orthotopic tumors at 4 weeks, following inoculation of *NR4A1*-null M231 cells versus parental controls. Each dot represents a tumor specimen. ***P<0.001 by two-tailed Student's t-Test, n=6. **(F)** Bar graphs showing RNA quantitation of ectopic *NR4A1* overexpression (OE) in BRx142 and BRx82 CTCs. Statistical significance was assessed by two-tailed Student's t-Test. ***P<0.001, n=2. **(G)** *In vitro* cell proliferation of BRx142 CTCs with ectopic *NR4A1* overexpression (OE), compared with parental control, showing only modest proliferative advantage compared with the demonstrated *in vivo* phenotype. Statistical significance was assessed by two-tailed Student's t-Test. *P<0.05, n=4. **(H)** Representative images of TUNEL assays showing reduction in apoptosis in the *NR4A1*-overexpressing BRx142 CTC-derived orthotopic tumors. Arrows indicate apoptotic cells. Scalebar, 50 μM. **(I)** Quantification of positive TUNEL signal in *NR4A1*-overexpressing (OE) BRx142 CTC-derived orthotopic tumors (day 97), compared with control, showing a marked reduction in apoptosis. Error bar denotes SEM. ****P<0.0001 by two-tailed Student's t-Test, n>300 single nuclei. **(J)** Heatmaps showing cooperative cell killing by increasing doses of the NR4A1 antagonist DIM-C-pPhCO$_2$Me (NR4A1-i) together with the DNA damaging chemotherapy Doxorubicin, but not with the CDK4/6 inhibitor Palbociclib, in both BRx142 and BRx82 CTCs. Color key from red to green indicates number of viable cells from high to low, respectively. **(K)** Scatter plots showing pairwise correlation of genebody ATAC-seq signal among three IEGs (*NR4A1*, *FOS*, *EGR1*) across all TCGA cancer types. Spearman's correlation coefficient (ρ) and p-value are shown. **(L)** Bar graph showing the percentage of breast cancer patients with cancers of different molecular subtypes (PAM50) showing high or low *FOS* genebody chromatin accessibility. *P<0.05 by Fisher exact test. **(M)** Bar graph showing lower pathologic tumor stages (AJCC) in breast cancers with high *FOS* genebody chromatin accessibility. *P<0.05 by Fisher exact test. **(N)** Box plots showing GSVA analysis of different pathways in TCGA primary tumors with high (n=237) or low (n=140) *NR4A1* genebody accessibility. **P<0.01; ****P<0.0001, by two-sided Welch's t-test. **(O)** IGV tracks showing ATAC-seq signal at murine IEG (*Nr4a1, Fos, Fosb, Egr1*) genebody and 3'-UTR regions (highlighted in shaded yellow) in mouse fetal or adult mammary gland cells. Original ATAC-seq data derived from (Dravis et al., 2018). **(P)** IGV tracks showing gain of ATAC-seq signal at IEG (*FOS, FOSB* and *JUN*) genebody and 3'-UTR regions (highlighted in shaded yellow) in different human CD8 positive T cell subsets upon cytokine stimulation. ATAC-seq data is reanalyzed from (Calderon et al., 2019).

Supplementary Figure Legend References

Calderon, D., Nguyen, M.L.T., Mezger, A., Kathiria, A., Muller, F., Nguyen, V., Lescano, N., Wu, B., Trombetta, J., Ribado, J.V*., et al.* (2019). Landscape of stimulation-responsive chromatin across diverse human immune cells. Nat Genet *51*, 1494-1505.

Dravis, C., Chung, C.Y., Lytle, N.K., Herrera-Valdez, J., Luna, G., Trejo, C.L., Reya, T., and Wahl, G.M. (2018). Epigenetic and Transcriptomic Profiling of Mammary Gland Development and Tumor Models Disclose Regulators of Cell State Plasticity. Cancer Cell *34*, 466-482 e466.

Jordan, N.V., Bardia, A., Wittner, B.S., Benes, C., Ligorio, M., Zheng, Y., Yu, M., Sundaresan, T.K., Licausi, J.A., Desai, R*., et al.* (2016). HER2 expression identifies dynamic functional states within circulating breast cancer cells. Nature *537*, 102-106.

Lawson, D.A., Bhakta, N.R., Kessenbrock, K., Prummel, K.D., Yu, Y., Takai, K., Zhou, A., Eyob, H., Balakrishnan, S., Wang, C.Y*., et al.* (2015). Single-cell analysis reveals a stem-cell program in human metastatic breast cancer cells. Nature *526*, 131-135.